

## Article

# Insights into the Electronic, Optical, and Anti-Corrosion Properties of Two-Dimensional ZnO: First-Principles Study

Fatma Abd Elwahab<sup>1,2</sup>, Nahed H. Teleb<sup>3,4</sup>, Hazem Abdelsalam<sup>3,5,\*</sup> , Omar H. Abd-Elkader<sup>6,\*</sup>   
and Qinfang Zhang<sup>3,\*</sup> 

- <sup>1</sup> Solar and Space Research Department, National Research Institute of Astronomy and Geophysics (NRIAG), Helwan, Cairo 11421, Egypt; fatma.abdelwahab@nriag.sci.eg  
<sup>2</sup> Physics Department, Faculty of Women for Arts, Science, and Education, Ain Shams University, Cairo 11757, Egypt  
<sup>3</sup> School of Materials Science and Engineering, Yancheng Institute of Technology, Yancheng 224051, China; n\_sleam@yahoo.com  
<sup>4</sup> Electron Microscope and Thin Films Department, National Research Centre, El-Buhouth Str., Dokki, Giza 12622, Egypt  
<sup>5</sup> Theoretical Physics Department, National Research Centre, El-Buhouth Str., Dokki, Giza 12622, Egypt  
<sup>6</sup> Department of Physics and Astronomy, College of Science, King Saud University, P.O. Box 2455, Riyadh 11451, Saudi Arabia  
\* Correspondence: hazemabdelhameed@gmail.com (H.A.); omabelkader7@ksu.edu.sa (O.H.A.-E.); qfangzhang@gmail.com (Q.Z.)

**Abstract:** The electronic, optical, and anticorrosion properties of planer ZnO crystal and quantum dots are explored using density functional theory calculations. The calculations for the finite ZnO quantum dots were performed in Gaussian 16 using the B3LYP/6-31g level of theory. The periodic calculations were carried out using VASP with the plane wave basis set and the PBE functional. The subsequent band structure calculations were performed using the hybrid B3LYP functional that shows accurate results and is also consistent with the finite calculations. The considered ZnO nanodots have planer hexagonal shapes with zigzag and armchair terminations. The binding energy calculations show that both structures are stable with negligible deformation at the edges. The ZnO nanodots are semiconductors with a moderate energy gap that decreases when increasing the size, making them potential materials for anticorrosion applications. The values of the electronic energy gaps of ZnO nanodots are confirmed by their UV-Vis spectra, with a wide optical energy gap for the small structures. Additionally, the calculated positive fraction of transferred electrons implies that electron transfer occurs from the inhibitor (ZnO) to the metal surface to passivate their vacant d-orbitals, and eventually prevent corrosion. The best anti-corrosion performance was observed in the periodic ZnO crystal with a suitable energy gap, electronegativity, and fraction of electron transfer. The effects of size and periodicity on the electronic and anticorrosion properties are also here investigated. The findings show that the anticorrosion properties were significantly enhanced by increasing the size of the quantum dot. Periodic ZnO crystals with an appropriate energy gap, electronegativity, and fraction of electron transfer exhibited the optimum anticorrosion performance. Thus, the preferable energy gap in addition to the most promising anticorrosion parameters imply that the monolayer ZnO is a potential candidate for coating and corrosion inhibitors.

**Keywords:** two dimensional ZnO; quantum dots; periodic lattice; DFT; electronic and optical properties; anticorrosion properties; coating



**Citation:** Elwahab, F.A.; Teleb, N.H.; Abdelsalam, H.; Abd-Elkader, O.H.; Zhang, Q. Insights into the Electronic, Optical, and Anti-Corrosion Properties of Two-Dimensional ZnO: First-Principles Study. *Crystals* **2024**, *14*, 179. <https://doi.org/10.3390/cryst14020179>

Academic Editors: Antonio Frontera and Vladislav V. Kharton

Received: 12 January 2024

Revised: 29 January 2024

Accepted: 8 February 2024

Published: 11 February 2024



**Copyright:** © 2024 by the authors. Licensee MDPI, Basel, Switzerland. This article is an open access article distributed under the terms and conditions of the Creative Commons Attribution (CC BY) license (<https://creativecommons.org/licenses/by/4.0/>).

## 1. Introduction

Traditional bulk inorganic semiconductors composed of elements from groups III to V, such as Si or Ge, started to take over as the dominating materials in electronics in the middle of the 20th century [1]. A new electronic revolution is under way, as we study a new class

of materials commonly referred to as organic semiconductors (OSCs) [2]. As yet, organic semiconductors show promise due to their low cost, flexibility, and ease of manufacturing over a broad area. It is still important to make more advancements in the performance of both materials and devices, as well as the changeable optoelectronic qualities that can be altered via chemical structure [3]. Research on 2D materials can be used in a variety of ways to generate future solutions to overcome the difficulties with OSCs [3]. One of the key aspects that affect a material's qualities is its dimension. According to dimensions, materials are classified into: (1) zero-dimensional (0D), for example, fullerene, nanoclusters, and quantum dots; (2) one-dimensional ones, for example, nanowires, nanofibers, or nanorods (carbon nanotubes); (3) two-dimensional ones, for example, nanosheets or thin films, such as graphene and silicene; and (4) three-dimensional (3D) complex forms, for example, graphite or diamond [4,5].

Two-dimensional materials (2D) are crystalline solids made up of one or more atomic layers [6,7]. For instance, graphene is an atomically thick layer of carbon atoms tightly bound in a hexagonal honeycomb lattice. In particular, 2D materials are perfect for improving physicochemical characteristics and developing functions at the atomic scale by chemical modification, element doping, thickness regulation, and heterostructure formation, all of which is challenging to accomplish with bulk materials [8,9]. Due to the exceptional features of 2D materials, they are used in various applications, such as electronics/optoelectronics [10], energy storage [11], sensors [8], and catalysis [9]. As a result, a variety of 2D materials, including graphene, graphitic carbon nitride (g-C<sub>3</sub>N<sub>4</sub>) [12], hexagonal boron nitride (hBN) [13], black phosphorus (BP) [14], metal nitrides/carbides (Mxenes) [15], transition metal dichalcogenides (TMDs) [16], layered double hydroxide (LDH) [17], and Mxenes [18], have been extensively investigated. Additionally, 2D materials based on group III elements, such as indium oxide (InO) and aluminum nitride (AlN), have been studied [19,20]. Santos et al. explored 2D InO with different stoichiometry [19]. They discovered that 2D InO with an InSe-type structure and its distinctive In–In distances closely match available experimental findings. Filho et al. also investigated the formation, stability, and electronic properties of Self-Induced Core–Shell InAlN Nanorods [20]. Because of the challenging issues with these 2D materials, for example, the low absorptivity and zero bandgap in graphene, researchers are focusing on structural modification as a way to resolve these drawbacks [21]. These drawbacks can be solved by converting these 2D semiconductor materials to 0D or quantum dots to produce new, inexpensive, and effective materials with novel features as a result of quantum confinement and substantial edge effects [12]. Via quantum confinement, a finite energy gap can be opened in graphene by converting it to a graphene quantum dot. The value of this energy gap is inversely proportional to the size of the quantum dot. The edge type also has a significant effect on the electronic and magnetic properties of graphene quantum dots, as reported in triangulene [22]. Additional control over the electronic, optical, and magnetic characteristics of 2D quantum dots (2D-QDs) can be achieved by chemical functionalization, doping, layer stacking, and electric field [23–25]. Many 2D-QDs, including graphene, silicene, phosphorene, MoS<sub>2</sub>, and hBN-QDs, have been shown to exhibit broadly adjustable photoluminescence due to their size-dependent electronic and optical properties. 2D-QDs show quantum confinement in all three dimensions [26–28]. As a result, QDs are promising for a variety of applications such as electronics [29], optical [30], spintronics [31], bioimaging [32], sensors [33], photovoltaics [34], and energy storage [35].

In the present work, we study the structural stability of planer zinc oxide (ZnO) quantum dots using density functional theory (DFT) calculations. Moreover, the electronic, optical, and anticorrosion properties are investigated. To generalize the current work, we extend the calculations to include quantum dots of different sizes and periodic ZnO crystals. It is worth noting that ZnO nanomaterials have drawn significant interest as potential anticorrosive agents compared to conventional anticorrosion substances such as calcium nitrite and organic inhibitors, due to their remarkable proprieties [36–39]. They offer excellent resistance to corrosion, high thermal stability, a tunable band structure,

optical transparency, hydrophobic characteristics, and safety [40]. For instance, calcium nitrite exhibits good corrosion inhibition of steel in concrete; however, it is toxic and very costly [37]. Additionally, organic coatings suffer from hydrophilicity and other drawbacks related to the organic matrix structure [41]. However, as a result of global efforts to produce environmentally acceptable and nontoxic coatings for the prevention of corrosion, research is being conducted to overcome these drawbacks. One of the more promising methods is to combine organic and inorganic functionalities in one coating system. This approach not only ensures better anticorrosion performance, but also addresses the shortcomings of the organic matrix [42,43]. Moreover, ZnO nanoparticles are excellent candidates for antimicrobial coatings due to their low toxicity, excellent biocompatibility to human tissues, high abundance, cost-effectiveness, and high photocatalytic efficiency in killing different infectious organisms [44]. Further, the flexible tunability of the electronic properties of ZnO, such as conductivity control by introducing defects in the ZnO structure, is favorable for coatings. For instance, Sakellis determined the activation volumes in ZnO using a thermodynamic model and different experimental data. The calculated activation volumes match the values found in the experiments [45]. The ZnO quantum dots considered in this work have two forms: hexagonal shape with zigzag edges (ZHEX) and armchair edges (AHEX). The results show that two-dimensional ZnO quantum dots and their periodic lattice are promising candidates for use in coating applications due to their attractive anticorrosion properties. The paper is organized as follows: Section 2 introduces the computational model, Section 3 provides the results and discussion, and Section 4 concludes.

## 2. Computational Model

The electronic, optical, and anticorrosion properties of 2D-ZnO quantum dots are investigated using density functional theory (DFT) calculations, as implemented in Gaussian 16 software [46]. The computations are performed using the 6–31 g basis set [47], which provides an accurate prediction of the molecular properties of the different nanosystems and has minimal computational complexity [48]. The hybrid functional (B3LYP) is employed in this work [49], which facilitates a good description of the electronic properties of various different systems [50,51]. The optical properties of 2D-ZnO quantum dots are investigated using time-dependent DFT (TD-DFT) calculations for the first twenty excited states. From the TD-DFT calculations, the UV-Vis can be simulated and the dominant optical transition can be identified. The quantum dots under consideration have been thoroughly optimized by minimizing energy and using a self-consistent field (SCF) convergence threshold of  $10^{-8}$ . This means that for the SCF to converge, the density matrix must change by less than  $10^{-6}$  at its maximum and less than  $10^{-8}$  at its root-mean-square (RMS). The periodic DFT calculations were carried out using Vienna ab initio simulation software (VASP) [52,53]. In the Perdew–Burke–Ernzerhof (PBE) functional, generalized gradient approximation (GGA) is used to explain the correlation and electron exchange [54]. For band structure calculations, we used the hybrid B3LYP functional so as to be consistent with the calculations considered for the finite quantum dots. This also shows a better representation of the electronic structure of the 2D ZnO lattice compared to other functionals, such as HSE06. The cutoff energy of the plane wave was chosen to be 520 eV. The energy and forces acting on individual atoms were converged according to the following criteria:  $10^{-5}$  eV and  $-0.01$  eV/Å, respectively. For the optimization and PDOS computations, a  $10 \times 10 \times 1$  gamma-centered K-point mesh was considered.

## 3. Results and Discussions

### 3.1. Structure Stability

The considered 2D ZnO quantum dots have two morphologies: hexagonal with zigzag edges (ZHEX) and hexagonal with armchair edges (AHEX). All edge atoms are passivated with H-atoms, as shown in Figure 1, to decrease possible deformations at the edges. Table 1 lists the optimal bond lengths and binding energies ( $E_B$ ) for each structure. According to Table 1, the H–O, H–Zn, and Zn–O bond lengths of AHEX–ZnO are 0.97–0.97 Å,

1.62–1.64 Å, and 1.90–1.98 Å, respectively, whereas those of ZHEX–ZnO are 0.96–0.97 Å, 1.62–1.63 Å and 1.88–2.06 Å. The lower bond lengths in Zn–O bonds come from surface atoms, while the higher bond lengths are observed at the edges. This is mainly a result of higher deformations at the edges after optimization. It is observed that ZHEX–ZnO quantum dots have slightly higher Zn–O bond lengths at the edges compared to those of AHEx–ZnO, which implies higher structural changes in the former.

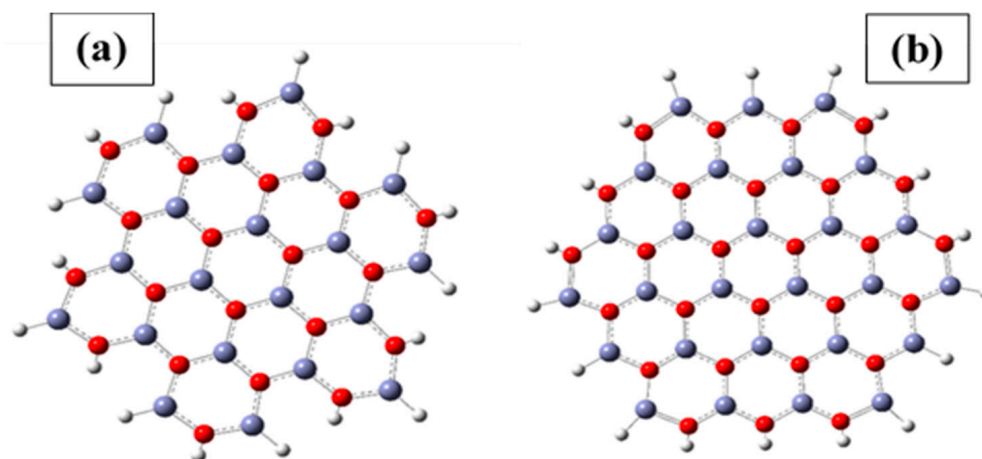


**Figure 1.** The optimized structures: (a) armchair–hexagonal ZnO (AHEx–ZnO) and (b) zigzag–hexagonal ZnO (ZHEX–ZnO). Red spherical atoms represent O atoms and Zn atoms are represented by bluish-white spheres.

**Table 1.** The optimized bond lengths and the binding energies ( $E_B$ ) of AHEx–ZnO and ZHEX–ZnO–H.

Structure	Bond Lengths (Å)			Binding Energy ( $E_B$ ) (eV)
	H–O	H–Zn	Zn–O	
AHEx–ZnO	0.971–0.974	1.615–1.640	1.897–1.977	−0.16
ZHEX–ZnO	0.969–0.970	1.622–1.631	1.877–2.056	−0.15

Negative values of the binding energy ( $E_B$ ) provide evidence for the energetic stability of the 2D–ZnO QDS, which is computed as:

$$E_B = \frac{E_c - (n_{Zn}E_{Zn} + n_{H}E_H + n_{O}E_O)}{N} \quad (1)$$

where  $E_C$  is the ground state energy of the compound, and  $E_{Zn}$ ,  $E_O$  and  $E_H$  are the ground state energies of Zn, O, and H, respectively.  $N$  is the total number of atoms and  $n$  is the number of individual atoms (Zn, O, or H). The values of the binding energy in Table 1 are negative with moderate values equal to −0.16 eV for AHEx–ZnO and −0.15 eV for ZHEX–ZnO. These negative values ensure that the considered ZnO quantum dots, namely, ZHEX and AHEx, are energetically stable with respect to their constituting atoms. Table 1 shows that AHEx–ZnO has more negative binding energy compared to ZHEX–ZnO. Therefore, AHEx–ZnO is slightly more stable than ZHEX–ZnO, which could be a result of the lower structural changes at the edges in AHEx–ZnO, as discussed before.

### 3.2. Electronic Properties

The highest occupied molecular orbital (HOMO) and the lowest unoccupied molecular orbital (LUMO), which are crucial for defining the electronic properties of the systems under consideration, are also important when studying anticorrosion properties [55–57]. The HOMO energy ( $E_{HOMO}$ ) is correlated with a molecule’s ability to donate electrons to the empty molecular orbitals, while  $E_{LUMO}$  is associated with a molecule’s capability to

accept electrons. The electronic energy gap ( $E_g$ ) is given by the difference between  $E_{\text{HOMO}}$  and  $E_{\text{LUMO}}$ , which determines the system's optical and transport properties. As shown in Figure 2, the HOMO distributions of the AHEx-ZnO and ZHEX-ZnO are localized on Zn and O atoms. The localized distributions indicate that the electrons that form these orbitals are interactive and originate from single atoms. On the other hand, the LUMO of the AHEx-ZnO and ZHEX-ZnO are delocalized and distributed on both Zn and O atoms. The energy gap of AHEx-ZnO ( $E_g = 4.28$  eV) is higher than that of ZHEX-ZnO ( $E_g = 3.77$  eV). These energy gaps make the ZnO quantum dots a wide band gap semiconductor. With this energy gap and the interactive low energy states, it is expected that ZnO nanodots will show attractive anti-corrosion features.

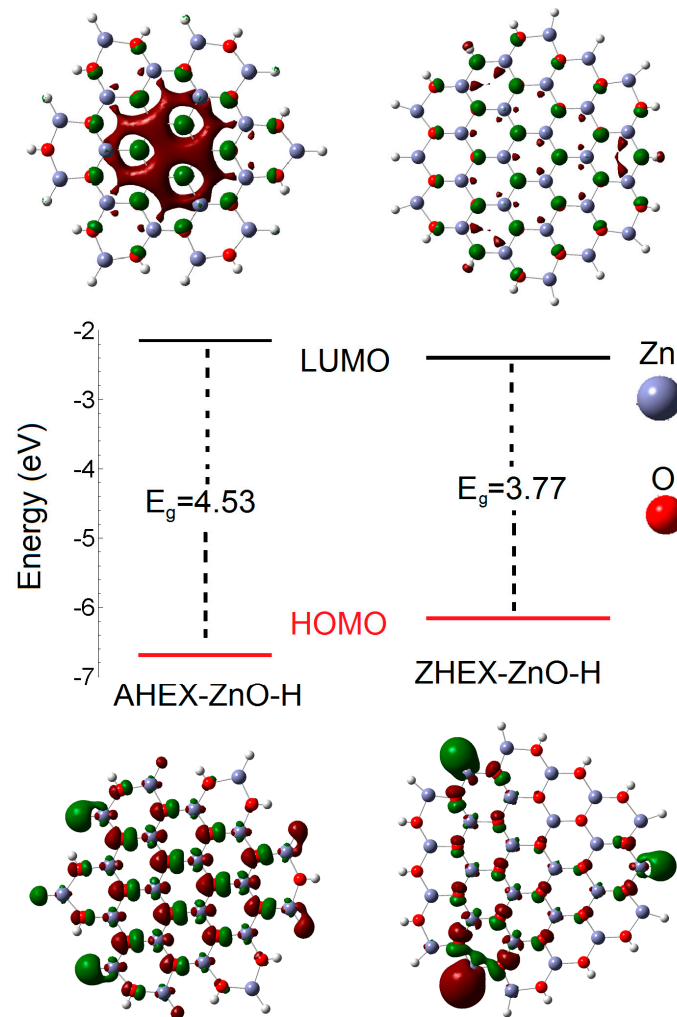


**Figure 2.** The distributions of the highest occupied/lowest unoccupied molecular orbitals (HOMO/LUMO) of the selected AHEx and ZHEX ZnO quantum dots. The electronic energy gaps and the energies of the HOMO and LUMO are also indicated.

### 3.3. Anticorrosion Performance

The energies of the LUMO ( $E_{\text{LUMO}}$ ) and the HOMO ( $E_{\text{HOMO}}$ ) are used to calculate important quantum stability chemical (QSC) parameters of the selected quantum dots, such as the electronic energy gap ( $\Delta E$ ), global hardness ( $\eta$ ), global softness ( $\sigma = 1/\eta$ ), and electronegativity ( $\chi$ ) [58]. The equations used to obtain these QSC parameters are given below:

$$\Delta E = E_{\text{LUMO}} - E_{\text{HOMO}} \quad (2)$$

$$\eta = \frac{\Delta E}{2} \quad (3)$$

$$\sigma = \frac{1}{\eta} \quad (4)$$

$$\chi = \frac{(E_{LUMO} + E_{HOMO})}{2} \quad (5)$$

The higher  $E_{HOMO}$  value of hydrogenated ZHEX–ZnO indicates that it has a greater ability to donate electrons to the metal surface. On the other hand, the more negative value of  $E_{LUMO}$  for AHEX–ZnO signifies a greater ability to accept electrons from the metal surface, as presented in Table 2. The energy gap ( $\Delta E = E_{LUMO} - E_{HOMO}$ ) is a crucial parameter for studying the inhibitor molecule's reactivity towards adsorption on the metallic surface [57]. The energy gap of AHEX–ZnO is relatively high (4.53 eV), but ZHEX–ZnO has a moderate energy gap equal to 3.77 eV that facilitates interactions with the metal. Additionally, the electron-donating capability of the inhibitor is determined by electronegativity ( $\chi$ ), which can be obtained from Equation (5). An effective restricting capability is provided by the inhibitor with a lower  $\chi$  (a higher tendency to donate electrons). Then,  $\chi$  of ZHEX–ZnO is suitable for corrosion inhibition because it exhibits higher electron donation. Moreover, other crucial variables that assess the stability and reactivity of the selected compounds are the global hardness ( $\eta$ ) and global softness ( $\sigma$ ). The hardness ( $\eta$ )/softness ( $\sigma$ ) of the AHEX–ZnO compound is slightly higher/lower than that of ZHEX–ZnO. Also, the fraction of transferred electrons between the inhibitor and metal surface ( $\Delta N$ ) is a good indicator of the strength of interaction between inhibitor and metals.  $\Delta N$  can be calculated according to the following equation [59],

$$\Delta N = \frac{\chi_{Fe} - \chi_{inh}}{2(\eta_{Fe} + \eta_{inh})} \quad (6)$$

where  $\chi_{Fe}$  and  $\chi_{inh}$  are the electronegativity values of iron and the inhibitor, respectively.  $\eta_{Fe}$  and  $\eta_{inh}$  are the hardness of the Fe ( $\eta_{Fe} = 0$  because  $E_{LUMO} = E_{HOMO}$  for bulk metal) and the inhibitor, respectively. In this investigation, the theoretical value of  $\chi_{Fe}$  (7 eV/mol) is obtained from DFT calculations for the Fe (110) surface [60]. The positive values of  $\Delta N$  imply that the electrons transfer from the ZnO nanodots (inhibitors) to the metal surface. Accordingly, the ZnO nanodots will donate electrons to the vacant d-orbital of the metal, which finally passivate these orbitals and prevent corrosion. As listed in Table 2, the positive values of  $\Delta N$  of both AHEX–ZnO and ZHEX–ZnO indicate that they can donate electrons to the vacant d-orbital of the metal, facilitating the formation of adsorptive bonds that finally passivate these orbitals and prevent corrosion.

**Table 2.** The quantum chemical parameters set for the selected molecular structures AHEX–ZnO and ZHEX–ZnO–H. Namely, the LUMO energy ( $E_{LUMO}$ ), the HOMO energy ( $E_{HOMO}$ ), global hardness ( $\eta$ ), global softness ( $\sigma = 1/\eta$ ), electronegativity ( $\chi$ ), and fraction of electron transfer.

Structure	$E_{LUMO}$ (eV)	$E_{HOMO}$ (eV)	$\Delta E$ (eV)	$\eta$ (eV)	$\sigma$ (eV <sup>-1</sup> )	$\chi$ (eV)	$\Delta N$
AHEX–ZnO	−2.17	−6.70	4.53	2.27	0.44	4.44	0.56
ZHEX–ZnO	−2.39	−6.17	3.77	1.89	0.53	4.28	0.72
4ZHEX–ZnO	−2.71	−5.83	3.12	1.56	0.64	4.27	0.88
5ZHEX–ZnO	−3.06	−5.38	2.32	1.16	0.86	4.22	1.19
ZnO-Crystal	0.78	−2.65	3.43	1.72	0.58	0.94	1.76

To study the important effects of size and periodicity on the electronic and anti-corrosion properties, we performed additional calculations on ZHEX–ZnO with a higher number of atoms—specifically, 4ZHEX–ZnO with four-edge hexagons and 5ZHEX–ZnO with five-edge hexagons, as seen in Figure S1. The periodic calculations on the ZnO crystal are also considered, and the discussion of its electronic properties is presented in the Supplementary Materials and Figure S2. It is observed that the values of the energy gaps

are decreased from 3.77 eV by increasing the size, which is mainly a result of the quantum confinement and the edges. The energy gaps of the four and five ZHEX are even lower than the energy gap (3.34 eV) of the periodic ZnO crystal, which contradicts the quantum confinement effect but can be explained by the edge effect. The distributions of the HOMO and LUMO of 4ZHEX–ZnO and 5ZHEX–ZnO on the edges indicate their origin from the interactive electrons at the edge atoms that decrease the energy gap.

The effect of size and periodicity on the  $E_{\text{HOMO}}$  shows a steady shift toward higher values when increasing the size, which is preferable for inhibitor materials because it ensures an improved ability to donate electrons to the metals. Moreover, the electronegativity decreases, reaching its minimum value in the ZnO crystal, confirming the elevated electron donation tendency in the periodic ZnO. The last indicator, showing the enhanced anticorrosion properties of the ZnO crystal compared to finite ZnO quantum dots, is the highest value of electron transfer, namely,  $\Delta N = 1.76$ .

### 3.4. Molecular Electrostatic Potentials (MEP)

Molecular Electrostatic Potential (MEP) shapes or surfaces have been widely used to analyze and predict molecular behavior, which helps in identifying reaction sites. MESP is effective because it can relate to how the total charge distribution influences the structure's electronegativity, dipole moment, partial charges, and chemical reactivity. MEPs can be categorized as being reactive with either electrophiles or nucleophiles. In contrast to negatively charged electrophiles, which have high potentials and no electrons, positively charged nucleophiles have low potentials and abundant electrons. A color map representing various MESP values appears on the surface of the molecule, with the colors arranged in ascending order: red > orange > yellow > green > blue. At MESP interfaces, the richest charge zone (negatively) is indicated by the color red, whereas the poorest charge region (positively) is indicated by the color blue, and the absence of electrostatic potential (neutral) is represented by the color green. In the 2D ZnO quantum dots that have been selected, the negative area (red color) is concentrated around O atoms, demonstrating that these are electrophilic locations. The positive (blue-colored) zones for AHEx–ZnO and AHEx–ZnO include all of the Zn and H atoms, proving that these locations are sensitive to nucleophilic activation, as shown in Figure 3. Therefore, the 2D ZnO quantum dots have abundant active sites on both their surfaces and edges that make them promising applicants for different applications, including gas sensors, catalysts, and coatings.

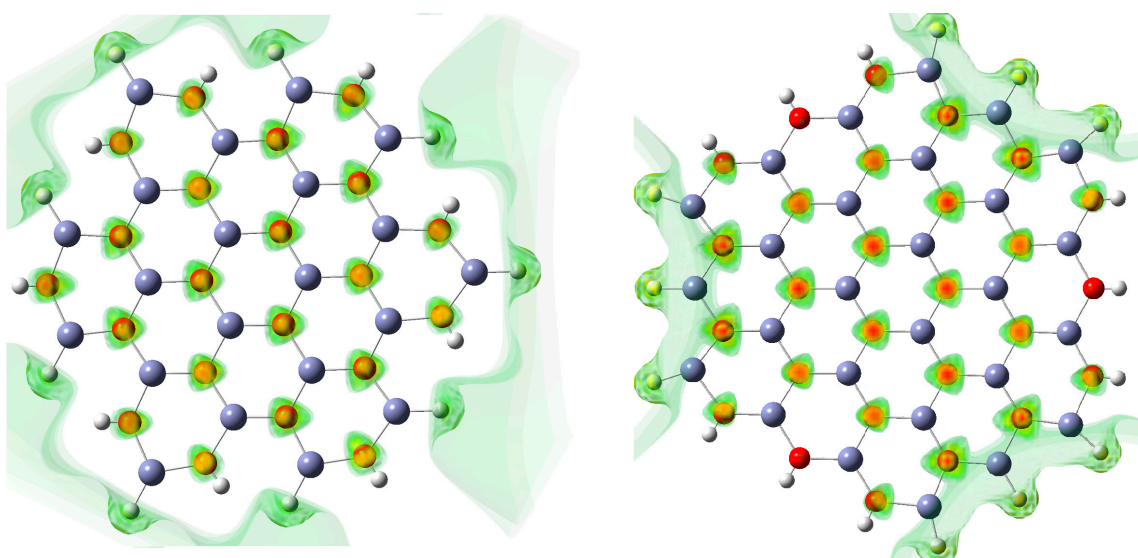


**Figure 3.** Electrostatic potential maps for the selected ZnO quantum dots with armchair (left side) and zigzag (right side) edge terminations.

### 3.5. UV-Vis Absorption Spectra

We examine the UV-Vis absorption spectra of AHEX-ZnO and ZHEX-ZnO in this section. The optical spectra are presented in Figure 4, and the related absorption parameters, such as excited state (ES), transition energy ( $\Delta E$ ), and oscillator strength ( $f$ ), are given in Table 3. According to Figure 4, the dominant absorption peaks for ZHEX-ZnO and AHEX-ZnO nanodots are located at 326 nm and 316 nm, respectively. This indicates that both ZHEX-ZnO and AHEX-ZnO are semiconductors, with wide optical band gaps of 3.80 and 3.93 eV, respectively.

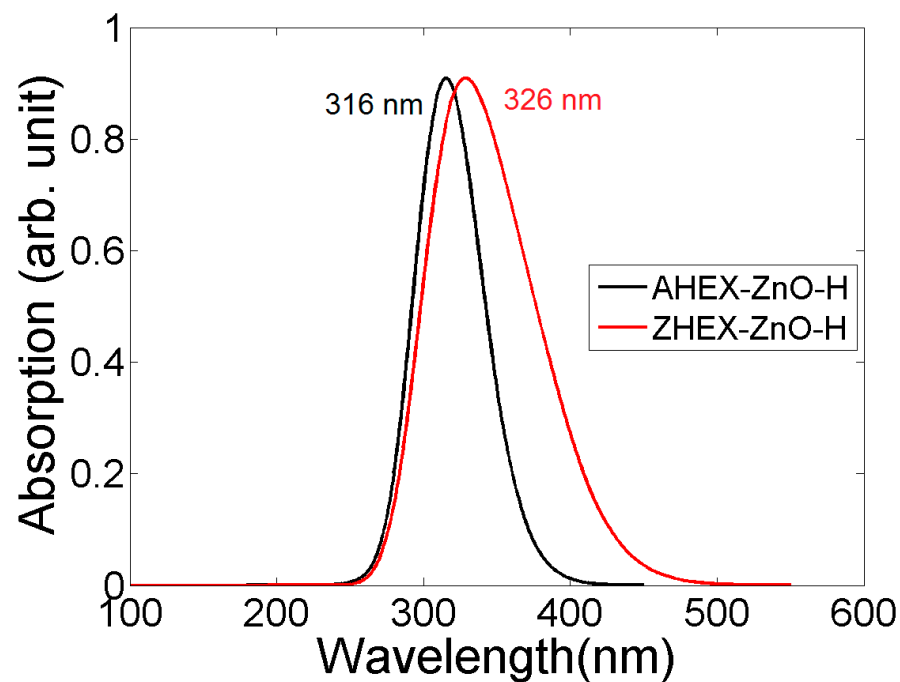


**Figure 4.** The computed absorption spectra of AHEX-ZnO and ZHEX-ZnO quantum dots. The wavelength of the main absorption peak is added to the plot.

**Table 3.** Useful absorption parameters, including the excited state (ES), transition wavelength ( $\lambda$ ), electronic transitions (ET), and transition energy ( $\Delta E$ ) oscillator strength ( $f$ ).

Absorption Parameters									
ES	ET	$\Delta E$ (eV)	$\lambda$ (nm)	$f$	ES	ET	$\Delta E$ (eV)	$\lambda$ (nm)	$f$
AHEX-ZnO					ZHEX-ZnO-H				
1	H $\rightarrow$ L	3.93	316	0.46	8	H-11 $\rightarrow$ L H-7 $\rightarrow$ L H-4 $\rightarrow$ L H-2 $\rightarrow$ L	3.80	326	0.34
2	H-2 $\rightarrow$ L	3.93	315	0.46	9	H-10 $\rightarrow$ L H-6 $\rightarrow$ L H-5 $\rightarrow$ L H-2 $\rightarrow$ L	3.80	326	0.34
4	H-4 $\rightarrow$ L H-3 $\rightarrow$ L	4.28	290	0.002	1	H $\rightarrow$ L	3.38	367	0.23

The main transitions for AHEX-ZnO are from the ground state ( $S_0$ ) to the first excited state and the second excited state at  $\lambda = 316$  nm (3.39 eV) and  $\lambda = 315$  nm, respectively. Both are composed of one main transition of H  $\rightarrow$  L, as given in Table 3. In the case of ZHEX-ZnO-H, the main excitations are from the ground state to the eighth and ninth

excited states at  $\lambda = 326$  nm (3.80 eV), and these are associated with four transitions, as detailed in Table 3. Also, the first excited states with H  $\rightarrow$  L transition make a considerable contribution to oscillator strength,  $f = 0.23$ .

#### 4. Conclusions

In this work, the structural stability, electronic, optical, and anticorrosion properties of planer ZnO quantum dots and their periodic lattice are explored using DFT calculations. The considered quantum dots have hexagonal shapes with zigzag and armchair terminations. The computed binding energies with moderate negative values indicate that the considered structures are energetically stable with respect to the constituting atoms. The electronic properties show also that these structures are semiconductors with a wide energy gap equal to  $\sim 4$  eV, which makes them promising candidates for use as corrosion inhibitors. The positive value of the fraction of transferred electrons ( $\Delta N$ ) implies that electrons will be transferred from the inhibitor to the metal surface to passivate their vacant orbitals and eventually prevent corrosion. This is confirmed by the electrostatic potential mapping, where we found that the Zn sites at the edges are active regions that can donate electrons. The UV-Vis spectra show that the ZnO quantum dot has a wide optical energy gap of  $\sim 4$  eV. The effects of size and periodicity on the electronic and anticorrosion properties are also investigated. The findings show that the anticorrosion properties are enhanced by increasing the size of the quantum dots. Periodic ZnO crystals with an appropriate energy gap, electronegativity, and fraction of electron transfer exhibit the optimal anti-corrosion performance. Therefore, the 2D ZnO nanomaterials with their wide energy gap and suitable anticorrosion parameters are a potential material for use in coatings and corrosion inhibition.

**Supplementary Materials:** The following supporting information can be downloaded at: <https://www.mdpi.com/article/10.3390/cryst14020179/s1>, Figure S1: The optimized structures of ZnO nanodots with four (4ZHEX-ZnO) and five (5ZHEXZnO) edge hexagons, see (a) and (d), respectively. The related HOMO and LUMO distributions of 4ZHEX-ZnO are shown in (b,c) and those for 5ZHEX-ZnO are shown in (e,f); Figure S2: (a) top view of the two-dimensional ZnO lattice with the unit cell indicated by the box. (b) the total and partial density of states. (c,d) The highest occupied/lowest unoccupied crystal. References [61,62] are cited in the Supplementary Materials.

**Author Contributions:** Conceptualization, H.A. and F.A.E.; methodology, H.A.; software, N.H.T. and Q.Z.; validation, O.H.A.-E., F.A.E. and N.H.T.; formal analysis, H.A.; investigation, H.A. and F.A.E.; resources, Q.Z. and O.H.A.-E.; data curation, F.A.E.; writing—original draft preparation, F.A.E. and H.A.; writing—review and editing, H.A., O.H.A.-E. and Q.Z.; visualization, H.A. and F.A.E.; supervision, Q.Z.; project administration, O.H.A.-E.; funding acquisition, Q.Z. and O.H.A.-E. All authors have read and agreed to the published version of the manuscript.

**Funding:** This work is supported by the National Natural Science Foundation of China (No. 12274361), the Natural Science Foundation of Jiangsu Province (BK20211361), and College Natural Science Research Project of Jiangsu Province (20KJA430004). This work is also supported by the Researchers Supporting Project number (RSP2024R468), King Saud University, Riyadh, Saudi Arabia.

**Data Availability Statement:** The original contributions presented in the study are included in the article and Supplementary Material, further inquiries can be directed to the corresponding authors.

**Conflicts of Interest:** The authors declare no conflicts of interest.

#### References

1. Morab, S.; Sundaram, M.M.; Pivrikas, A. Review on charge carrier transport in inorganic and organic semiconductors. *Coatings* **2023**, *13*, 1657. [CrossRef]
2. Brütting, W. Introduction to the physics of organic semiconductors. In *Physics of Organic Semiconductors*; Wiley: Hoboken, NJ, USA, 2005; pp. 1–14.
3. Yadav, S.; Jena, S.R.; MB, B.; Altaee, A.; Saxena, M.; Samal, A.K. Heterostructures of 2D materials-quantum dots (QDs) for optoelectronic devices: Challenges and opportunities. *Emergent Mater.* **2021**, *4*, 901–922. [CrossRef]

4. Sakthivel, R.; Keerthi, M.; Chung, R.-J.; He, J.-H. Heterostructures of 2D materials and their applications in biosensing. *Prog. Mater. Sci.* **2023**, *132*, 101024. [[CrossRef](#)]
5. Mas-Balleste, R.; Gomez-Navarro, C.; Gomez-Herrero, J.; Zamora, F. 2D materials: To graphene and beyond. *Nanoscale* **2011**, *3*, 20–30. [[CrossRef](#)] [[PubMed](#)]
6. Velický, M.; Toth, P.S. From two-dimensional materials to their heterostructures: An electrochemist's perspective. *Appl. Mater. Today* **2017**, *8*, 68–103. [[CrossRef](#)]
7. Duong, D.L.; Yun, S.J.; Lee, Y.H. van der Waals layered materials: Opportunities and challenges. *ACS Nano* **2017**, *11*, 11803–11830. [[CrossRef](#)]
8. Medina, H.; Li, J.-G.; Su, T.-Y.; Lan, Y.-W.; Lee, S.-H.; Chen, C.-W.; Chen, Y.-Z.; Manikandan, A.; Tsai, S.-H.; Navabi, A. Wafer-scale growth of wse2 monolayers toward phase-engineered hybrid wo x/wse2 films with sub-ppb no x gas sensing by a low-temperature plasma-assisted selenization process. *Chem. Mater.* **2017**, *29*, 1587–1598. [[CrossRef](#)]
9. Qu, Y.; Medina, H.; Wang, S.W.; Wang, Y.C.; Chen, C.W.; Su, T.Y.; Manikandan, A.; Wang, K.; Shih, Y.C.; Chang, J.W. Wafer scale phase-engineered 1T-and 2H-MoSe2/Mo core-shell 3D-hierarchical nanostructures toward efficient electrocatalytic hydrogen evolution reaction. *Adv. Mater.* **2016**, *28*, 9831–9838. [[CrossRef](#)]
10. Waleed, A.; Tavakoli, M.M.; Gu, L.; Wang, Z.; Zhang, D.; Manikandan, A.; Zhang, Q.; Zhang, R.; Chueh, Y.-L.; Fan, Z. Lead-free perovskite nanowire array photodetectors with drastically improved stability in nanoengineering templates. *Nano Lett.* **2017**, *17*, 523–530. [[CrossRef](#)]
11. Bollella, P.; Fusco, G.; Tortolini, C.; Sanzò, G.; Favero, G.; Gorton, L.; Antiochia, R. Beyond graphene: Electrochemical sensors and biosensors for biomarkers detection. *Biosens. Bioelectron.* **2017**, *89*, 152–166. [[CrossRef](#)]
12. Manikandan, A.; Chen, Y.-Z.; Shen, C.-C.; Sher, C.-W.; Kuo, H.-C.; Chueh, Y.-L. A critical review on two-dimensional quantum dots (2D QDs): From synthesis toward applications in energy and optoelectronics. *Prog. Quantum Electron.* **2019**, *68*, 100226. [[CrossRef](#)]
13. Xu, M.; Liang, T.; Shi, M.; Chen, H. Graphene-like two-dimensional materials. *Chem. Rev.* **2013**, *113*, 3766–3798. [[CrossRef](#)] [[PubMed](#)]
14. Liu, H.; Neal, A.T.; Zhu, Z.; Tomanek, D.; Ye, P.D. Phosphorene: A new 2D material with high carrier mobility. *arXiv* **2014**, arXiv:1401.4133.
15. Naguib, M.; Come, J.; Dyatkin, B.; Presser, V.; Taberna, P.-L.; Simon, P.; Barsoum, M.W.; Gogotsi, Y. MXene: A promising transition metal carbide anode for lithium-ion batteries. *Electrochem. Commun.* **2012**, *16*, 61–64. [[CrossRef](#)]
16. Tan, C.; Zhang, H. Two-dimensional transition metal dichalcogenide nanosheet-based composites. *Chem. Soc. Rev.* **2015**, *44*, 2713–2731. [[CrossRef](#)]
17. Lv, L.; Yang, Z.; Chen, K.; Wang, C.; Xiong, Y. 2D layered double hydroxides for oxygen evolution reaction: From fundamental design to application. *Adv. Energy Mater.* **2019**, *9*, 1803358. [[CrossRef](#)]
18. Gogotsi, Y.; Anasori, B. The rise of MXenes. *ACS Nano* **2019**, *13*, 8491–8494. [[CrossRef](#)]
19. dos Santos, R.B.; Rivelino, R.; Gueorguiev, G.K.; Kakanakova-Georgieva, A. Exploring 2D structures of indium oxide of different stoichiometry. *CrystEngComm* **2021**, *23*, 6661–6667. [[CrossRef](#)]
20. Alves Machado Filho, M.; Hsiao, C.-L.; Dos Santos, R.B.; Hultman, L.; Birch, J.; Gueorguiev, G.K. Self-Induced Core-Shell InAlN Nanorods: Formation and Stability Unraveled by Ab Initio Simulations. *ACS Nanosci. Au* **2022**, *3*, 84–93. [[CrossRef](#)]
21. Huang, M.; Wang, M.; Chen, C.; Ma, Z.; Li, X.; Han, J.; Wu, Y. Broadband black-phosphorus photodetectors with high responsivity. *Adv. Mater.* **2016**, *28*, 3481–3485. [[CrossRef](#)]
22. Pavliček, N.; Mistry, A.; Majzik, Z.; Moll, N.; Meyer, G.; Fox, D.J.; Gross, L. Synthesis and characterization of triangulene. *Nat. Nanotechnol.* **2017**, *12*, 308–311. [[CrossRef](#)] [[PubMed](#)]
23. Kabel, J.; Sharma, S.; Acharya, A.; Zhang, D.; Yap, Y.K. Molybdenum disulfide quantum dots: Properties, synthesis, and applications. *C* **2021**, *7*, 45. [[CrossRef](#)]
24. Prasannachandran, R.; Vineesh, T.V.; Anil, A.; Krishna, B.M.; Shaijumon, M.M. Functionalized phosphorene quantum dots as efficient electrocatalyst for oxygen evolution reaction. *ACS Nano* **2018**, *12*, 11511–11519. [[CrossRef](#)] [[PubMed](#)]
25. Abdelsalam, H.; Zhang, Q. Spintronic properties of 2D heterostructures from laterally connected graphene and hBN quantum dots. *Chem. Phys. Lett.* **2023**, *825*, 140591. [[CrossRef](#)]
26. Jin, S.H.; Kim, D.H.; Jun, G.H.; Hong, S.H.; Jeon, S. Tuning the photoluminescence of graphene quantum dots through the charge transfer effect of functional groups. *ACS Nano* **2013**, *7*, 1239–1245. [[CrossRef](#)] [[PubMed](#)]
27. Golovynskyi, S.; Datsenko, O.I.; Dong, D.; Lin, Y.; Golovynska, I.; Jin, Z.; Li, B.; Wu, H. MoS<sub>2</sub> monolayer quantum dots on a flake: Efficient sensitization of exciton and trion photoluminescence via resonant nonradiative energy and charge transfers. *Appl. Surf. Sci.* **2022**, *601*, 154209. [[CrossRef](#)]
28. Angizi, S.; Alem, S.A.A.; Azar, M.H.; Shayeganfar, F.; Manning, M.I.; Hatamie, A.; Pakdel, A.; Simchi, A. A comprehensive review on planar boron nitride nanomaterials: From 2D nanosheets towards 0D quantum dots. *Prog. Mater. Sci.* **2022**, *124*, 100884. [[CrossRef](#)]
29. Zhu, H.; Liu, A.; Xu, Y.; Shan, F.; Li, A.; Wang, J.; Yang, W.; Barrow, C.; Liu, J. Graphene quantum dots directly generated from graphite via magnetron sputtering and the application in thin-film transistors. *Carbon* **2015**, *88*, 225–232. [[CrossRef](#)]
30. Long, M.; Wang, P.; Fang, H.; Hu, W. Progress, challenges, and opportunities for 2D material based photodetectors. *Adv. Funct. Mater.* **2019**, *29*, 1803807. [[CrossRef](#)]

31. Abdelsalam, H.; Atta, M.M.; Saroka, V.A.; Zhang, Q. Anomalous magnetic and transport properties of laterally connected graphene quantum dots. *J. Mater. Sci.* **2022**, *57*, 14356–14370. [CrossRef]
32. Zheng, X.T.; Ananthanarayanan, A.; Luo, K.Q.; Chen, P. Glowing graphene quantum dots and carbon dots: Properties, syntheses, and biological applications. *Small* **2015**, *11*, 1620–1636. [CrossRef] [PubMed]
33. Sakr, M.A.; Saad, M.A.; Abdelsalam, H.; Abd-Elkader, O.H.; Aleya, L.; Zhang, Q. Two-Dimensional ZnS Quantum Dots for Gas Sensors: Electronic and Adsorption Properties. *J. Electron. Mater.* **2023**, *52*, 5227–5238. [CrossRef]
34. Abdelsalam, H.; Atta, M.M.; Osman, W.; Zhang, Q. Two-dimensional quantum dots for highly efficient heterojunction solar cells. *J. Colloid Interface Sci.* **2021**, *603*, 48–57. [CrossRef] [PubMed]
35. Wang, H.; Feng, H.; Li, J. Graphene and graphene-like layered transition metal dichalcogenides in energy conversion and storage. *Small* **2014**, *10*, 2165–2181. [CrossRef] [PubMed]
36. Marcus, P. *Corrosion Mechanisms in Theory and Practice*; CRC Press: Boca Raton, FL, USA, 2011.
37. de Rincon, O.T.; Perez, O.; Paredes, E.; Caldera, Y.; Urdaneta, C.; Sandoval, I. Long-term performance of ZnO as a rebar corrosion inhibitor. *Cem. Concr. Compos.* **2002**, *24*, 79–87. [CrossRef]
38. Al-Dahiri, R.H.; Turkustani, A.M.; Salam, M.A. The application of zinc oxide nanoparticles as an eco-friendly inhibitor for steel in acidic solution. *Int. J. Electrochem. Sci.* **2020**, *15*, 442–457. [CrossRef]
39. Kamburova, K.; Boshkova, N.; Boshkov, N.; Radeva, T. Composite coatings with polymeric modified ZnO nanoparticles and nanocontainers with inhibitor for corrosion protection of low carbon steel. *Colloids Surf. A Physicochem. Eng. Asp.* **2021**, *609*, 125741. [CrossRef]
40. Quadri, T.W.; Olasunkanmi, L.O.; Fayemi, O.E.; Ebenso, E.E. Utilization of ZnO-based materials as anticorrosive agents: A review. *Inorg. Anticorros. Mater.* **2022**, 161–182. [CrossRef]
41. Nazari, M.H.; Zhang, Y.; Mahmoodi, A.; Xu, G.; Yu, J.; Wu, J.; Shi, X. Nanocomposite organic coatings for corrosion protection of metals: A review of recent advances. *Prog. Org. Coat.* **2022**, *162*, 106573. [CrossRef]
42. Ammar, S.; Ramesh, K.; Vengadaesvaran, B.; Ramesh, S.; Arof, A.K. Formulation and characterization of hybrid polymeric/ZnO nanocomposite coatings with remarkable anti-corrosion and hydrophobic characteristics. *J. Coat. Technol. Res.* **2016**, *13*, 921–930. [CrossRef]
43. Shi, X.; Nguyen, T.A.; Suo, Z.; Liu, Y.; Avci, R. Effect of nanoparticles on the anticorrosion and mechanical properties of epoxy coating. *Surf. Coat. Technol.* **2009**, *204*, 237–245. [CrossRef]
44. Puspasari, V.; Ridhova, A.; Hermawan, A.; Amal, M.I.; Khan, M.M. ZnO-based antimicrobial coatings for biomedical applications. *Bioprocess Biosyst. Eng.* **2022**, *45*, 1421–1445. [CrossRef]
45. Sakellis, I. Determining the activation volumes in ZnO. *J. Appl. Phys.* **2012**, *112*, 013504. [CrossRef]
46. Frisch, M.E.; Trucks, G.; Schlegel, H.; Scuseria, G.; Robb, M.; Cheeseman, J.; Scalmani, G.; Barone, V.; Petersson, G.; Nakatsuji, H. Gaussian 16, Revision C. 01. 2016. Available online: <https://gaussian.com/citation/> (accessed on 10 January 2024).
47. Hehre, W.J.; Ditchfield, R.; Pople, J.A. Self-Consistent molecular orbital methods. XII. Further extensions of Gaussian—Type basis sets for use in molecular orbital studies of organic molecules. *J. Chem. Phys.* **1972**, *56*, 2257–2261. [CrossRef]
48. Yang, Y.; Weaver, M.N.; Merz, K.M., Jr. Assessment of the “6-31 + G\*\* + LANL2DZ” mixed basis set coupled with density functional theory methods and the effective core potential: Prediction of heats of formation and ionization potentials for first-row-transition-metal complexes. *J. Phys. Chem. A* **2009**, *113*, 9843–9851. [CrossRef] [PubMed]
49. Becke, A.D. Density-functional thermochemistry. I. The effect of the exchange-only gradient correction. *J. Chem. Phys.* **1992**, *96*, 2155–2160. [CrossRef]
50. Povie, G.; Segawa, Y.; Nishihara, T.; Miyauchi, Y.; Itami, K. Synthesis and size-dependent properties of [12], [16], and [24] carbon nanobelts. *J. Am. Chem. Soc.* **2018**, *140*, 10054–10059. [CrossRef]
51. Hegazy, M.A.; Ezzat, H.A.; Yahia, I.S.; Zahran, H.Y.; Elhaes, H.; Matar, H.; Ibrahim, M. Effect of Metal Oxides and Graphene Upon The Electronic Properties of Polyvinyl Alcohol. 2021, *preprint*. [CrossRef]
52. Kresse, G.; Hafner, J. Ab initio molecular dynamics for liquid metals. *Phys. Rev. B* **1993**, *47*, 558. [CrossRef]
53. Kresse, G.; Furthmüller, J. Efficient iterative schemes for ab initio total-energy calculations using a plane-wave basis set. *Phys. Rev. B* **1996**, *54*, 11169. [CrossRef]
54. Perdew, J.P.; Burke, K.; Ernzerhof, M. Generalized gradient approximation made simple. *Phys. Rev. Lett.* **1996**, *77*, 3865. [CrossRef]
55. Kushwaha, A.K.; Sahoo, M.R.; Ray, M.; Das, D.; Nayak, S.; Maity, A.; Sarkar, K.; Bhagat, A.N.; Pal, A.R.; Rout, T.K. Functional Pyromellitic Diimide as a Corrosion Inhibitor for Galvanized Steel: An Atomic-Scale Engineering. *ACS Omega* **2022**, *7*, 27116–27125. [CrossRef]
56. Radhi, A.H.; Du, E.A.; Khazaal, F.A.; Abbas, Z.M.; Aljelawi, O.H.; Hamadan, S.D.; Almashhadani, H.A.; Kadhim, M.M. HOMO-LUMO energies and geometrical structures effect on corrosion inhibition for organic compounds predict by DFT and PM3 methods. *NeuroQuantology* **2020**, *18*, 37. [CrossRef]
57. Zarrouk, A.; El Ouali, I.; Bouachrine, M.; Hammouti, B.; Ramli, Y.; Essassi, E.; Warad, I.; Aouniti, A.; Salghi, R. Theoretical approach to the corrosion inhibition efficiency of some quinoxaline derivatives of steel in acid media using the DFT method. *Res. Chem. Intermed.* **2013**, *39*, 1125–1133. [CrossRef]
58. Gece, G. The use of quantum chemical methods in corrosion inhibitor studies. *Corros. Sci.* **2008**, *50*, 2981–2992. [CrossRef]
59. Kokalj, A. Is the analysis of molecular electronic structure of corrosion inhibitors sufficient to predict the trend of their inhibition performance. *Electrochim. Acta* **2010**, *56*, 745–755. [CrossRef]

60. Kocalj, A. On the HSAB based estimate of charge transfer between adsorbates and metal surfaces. *Chem. Phys.* **2012**, *393*, 1–12. [[CrossRef](#)]
61. Lee, J.; Sorescu, D.C.; Deng, X. Tunable lattice constant and band gap of single-and few-layer ZnO. *J. Phys. Chem. Lett.* **2016**, *7*, 1335–1340. [[CrossRef](#)] [[PubMed](#)]
62. Zhao, Y.; Liu, N.; Zhou, S.; Zhao, J. Two-dimensional ZnO for the selective photoreduction of CO<sub>2</sub>. *J. Mater. Chem. A* **2019**, *7*, 16294–16303. [[CrossRef](#)]

**Disclaimer/Publisher’s Note:** The statements, opinions and data contained in all publications are solely those of the individual author(s) and contributor(s) and not of MDPI and/or the editor(s). MDPI and/or the editor(s) disclaim responsibility for any injury to people or property resulting from any ideas, methods, instructions or products referred to in the content.